Optics and Laser Technology 130 (2020) 106356

Contents lists available at ScienceDirect

Optics and Laser Technology

journal homepage: www.elsevier.com/locate/optlastec

Review

Large aperture diffractive optical telescope: A review

Haolin Zhang[a,b,c,d], Hua Liu[a,d,*], Wenbin Xu[b], Zhenwu Lu[b]

[a] Demonstration Center for Experimental Physics Education, College of Physics, Northeast Normal University, Changchun 130024, China
[b] Changchun Institute of Optics, Fine Mechanics and Physics, Chinese Academy of Sciences, Changchun, Jilin 130033, China
[c] University of Chinese Academy of Sciences, Beijing 100039, China
[d] Key Laboratory of Spectral Imaging Technology of Chinese Academy of Sciences, Xi'an 710119, China

HIGHLIGHTS

- We review the optical design principle of large aperture diffractive telescopes.
- DOE fabrication techniques are discussed and different DOEs are presented.
- Subaperture DOE stitching principle is presented and thoroughly discussed.
- 5 categories of representative diffractive telescopes are reviewed and compared.

ARTICLE INFO

Keywords:
Telescope
Diffractive optical element
Optical design
Aperture
Imaging system

ABSTRACT

Thanks to the recent development in diffractive optical element (DOE) fabrication technique, large aperture diffractive telescope systems have been tremendously studied to achieve high-resolution imaging. In this review, the universal optical design mechanism of a diffractive telescope system is initially elucidated, and the state-of-art progresses of large aperture diffractive optical telescopes are overviewed. Then, we analyze DOE lithography technique, from which we can fabricate DOEs on different substrates. Moreover, we also present subaperture stitching, so that we can obtain large aperture DOEs. Afterwards, different experimentally implemented ground-based diffractive telescope systems are reviewed by emphasizing their advantages. Finally, we propose the prospects with respect to the arising challenges in large aperture diffractive telescope systems.

1. Introduction

With the recent developments in large aperture freeform optical element design [1,2], high precision optical fabrication and testing [3–8], large aperture telescope systems are proposed to perform high-resolution imaging. For instance, they demonstrate great ability to perform astronomy observation, from which we can explore sophisticated physical phenomenon [9–11]. In particular, most large aperture telescope systems use an aspherical mirror as the primary aperture [12,13]. Unfortunately, great challenges are encountered in both mirror fabrication and testing accompanied by enlarging the aspherical mirror diameter. Under this scenario, large aperture diffractive optical element (DOE) based telescope systems [14], which use a DOE as the primary aperture, are proposed. The advantage of diffractive telescopes compared to traditional reflective telescopes are mainly manifested in two aspects. On the one hand, the telescope system weight can be dramatically reduced by fabricating DOE pattern on a low-weight substrate [15]. On the other hand, the transmissive DOE provides a loose surface shape tolerance [16,17], and this will alleviate the difficulties during surface fabrication and testing.

The concept of diffractive telescopes was firstly proposed by designing a monochromatic afocal Keplerian diffractive telescope using Seidel aberration correction [18]. Unfortunately, as the primary lens is a wavelength-dependent diffractive optical element, this telescope is not able to perform achromatic imaging, and thus, such scheme is not widely utilized. Under this scenario, Hyde et al. proposed a broadband spectral diffractive telescope system [14] by introducing Schupmann chromatic dispersion correction theory [19]. Their telescope contains two separate sections as a primary diffractive optical element and an eyepiece system. Here, the transparent large diameter diffractive element is implemented as the magnifying aperture, and the eyepiece is introduced as both the image receiver and the chromatic aberration corrector. Once the basic diffractive telescope scheme has been determined, different diffractive telescope systems were proposed to satisfy extensive applications. For instance, "Gen II" and "Gen III" prototypes designed by Koechlin et al. were used to achieve infrared

* Corresponding author at: Demonstration Center for Experimental Physics Education, College of Physics, Northeast Normal University, Changchun 130024, China.
E-mail address: liuhua_rain@aliyun.com (H. Liu).

https://doi.org/10.1016/j.optlastec.2020.106356
Received 21 June 2019; Received in revised form 10 May 2020; Accepted 12 May 2020
Available online 30 May 2020
0030-3992/

imaging (i.e., at 800 nm) [20,21] and UV imaging (i.e., at 260 nm) [22,23]. In the infrared imaging diffractive telescope, the DOE has a diameter of 200 mm and a focal length of 18 m. In the UV imaging diffractive telescope, the diameter of the DOE is 65 mm, and its focal length is 12.7 m. Nevertheless, both prototypes cannot guarantee a large field of view imaging. Hence, a compound diffractive telescope system, which combines compound eyes with diffractive optical elements, was presented by Liu et al. [24] to provide large field of view (FOV) imaging as 4.2°. However, these above-mentioned telescopes still cannot guarantee ultra-short wavelength imaging (i.e., ultra UV or X-ray imaging). Therefore, photon sieve based diffractive telescopes, which is feasible to both suppress higher order diffraction and focus super short wavelength, was illustrated by Anderson et al. by implementing a 0.1 m diameter, 1 m focal length antihole photon sieve [25,26]. Moreover, to achieve super high-resolution imaging, Atcheson et al. also proposed a large aperture MOIRE diffractive telescope [27-29]. In particular, the primary aperture in MOIRE system is a 5-meter diameter fragmentary DOE which consists of several stitched membrane subapertures. Here, MOIRE telescope demonstrated an imaging ability of NIIRS as 2.3 by selecting National Imagery Interpretability Rating Scale (NIIRS) as criteria [30]. However, subaperture stitching error of the primary aperture has not been considered. Therefore, Zhang et al. thoroughly investigated three-dimensional stitching error of a subaperture stitching diffractive lens by using a 300 mm diameter, three-belt deployed subaperture Fresnel lens [31]. What is more, they also assembled a 2 m focal length diffractive telescope by using that same subaperture stitching diffractive lens as the primary lens. Next, they also studied the influence of any stitching error to the imaging quality [32]. Finally, the image contrast deterioration of a diffractive telescope system, which is introduced by the long system length, was resolved by implementing a Cassegrain scheme in the diffractive telescope [32].

This paper is devoted to systematically review the techniques to implement a large aperture diffractive optical telescope system for high-resolution imaging. First of all, the designing principle of a diffractive telescope system is discussed by introducing chromatic aberration correction, from which we can broad the imaging spectral coverage. Secondly, we present optical lithography fabrication, from which we can obtain thin membrane or silicon substrate DOEs (i.e., Fresnel zone plates or photon sieves). Thirdly, we describe the feasibility of using subaperture stitching to obtain large aperture DOEs for high-resolution imaging. Finally, we review some representative diffractive telescope systems which have already been implemented. What is more, we also discuss and emphasize their system schemes and their corresponding advantages.

The outline of this review is listed as follows. In Section 2, the universal optical design principle of a diffractive telescope is thoroughly elucidated by applying Schupmann chromatic aberration correction theory. We also demonstrate that the undesired long optical length of a diffractive telescope system can be compacted by introducing a relay lens located between the primary diffractive lens and the chromatic dispersion correction lens. In Section 3, we mainly discuss different techniques to obtain large aperture DOEs. At the beginning, we explicate optical lithography and laser direct writing techniques to fabricate different DOEs acting as the primary apertures in diffractive telescope systems. To be more specific, we present the fabrication of both Fresnel zone plates and photon sieves. Afterwards, we introduce thin membrane DOEs, and we highlight the superiority of utilizing membranes to replace regular silicon substrates as DOEs. Finally, we demonstrate subaperture stitching principle. In principle, by implementing subaperture DOE stitching, we can obtain large aperture DOEs, so that we can achieve high-resolution imaging. In Section 4, different ground-based diffractive telescopes are reviewed. Note that any proposed telescope system is specialized for certain applications (i.e., high-resolution imaging, wide FOV imaging or turbulence-free imaging, *etc.*). The main conclusion and the potential prospects are provided in Section 5.

2. Optical design principle of a diffractive telescope system

2.1. Schupmann achromatic diffractive telescope system

In this section, we present the designing principle of a diffractive telescope. Moreover, we also demonstrate that by using Schupmann theory, we can eliminate the chromatic dispersion of a diffractive telescope system.

The Fresnel lens used as the primary lens in a diffractive telescope system has a focal length of f represented as Eq. (1) by ignoring the material dispersion [31],

$$f = \frac{D^2}{8\lambda N}, \tag{1}$$

where D is the diameter of the Fresnel lens, λ is the central wavelength of the incident light and N represents the numbers of the zone. From Eq. (1), we find that the focal length of a Fresnel lens varies within different input wavelengths, hence a Fresnel lens is only feasible to focus a narrow spectral bandwidth to the designed focal plane, but it will disperse the rest input wavelengths. Thus, we will see a diffusion spot on the designed focal plane if the incident light has a wide spectrum. On the other hand, to obtain an optical precision as $\pi/4$ (i.e., Rayleigh Criterion [33]), the spectral bandwidth range is restricted by Eq. (2) [14],

$$\left|\frac{\Delta\lambda}{\lambda}\right| \leqslant f_{number}\frac{\lambda}{D}, \tag{2}$$

where f_{number} is the f-number of the Fresnel lens.

In this case, we can say that a DOE can only focus a limited bandwidth. For instance, a DOE with its f_{number} of 100 and a central wavelength of 632 nm only provides a bandwidth limitation of 2.1×10^{-6} (i.e., the DOE diameter is 300 mm and the focal length as 30,000 mm). Note that such narrow bandwidth is not applicable because a wide spectrum is required in a telescope system to guarantee wide spectral imaging. Under this scenario, the chromatic dispersion aberration introduced by the Fresnel lens must be eliminated. Considering the limitation of the proposed compensation methods such as implementing sequential holographic diffractive elements [34–36], Schupmann chromatic aberration correction principle is proposed to compensate the diffractive telescope chromatic dispersion. Schupmann theory is demonstrated as below: any chromatic dispersion originated from an imperfect optical element can be compensated by introducing another optical element with a same optical scheme but inversed dispersion characteristic at the image plane of the original element. By using this principle, we can obtain achromatic imaging within the whole spectrum.

To implement a Schupmann compensation diffractive telescope, we use a large aperture DOE as the primary lens and its inversed diffractive lens as the chromatic compensator. Moreover, a convergent field lens is inserted between the two DOEs to image the first diffractive lens to coincide with the front surface of the compensator DOE. Note that only in this way the Schupmann condition can be satisfied. Finally, an eyepiece optical system is introduced behind the compensator DOE. This eyepiece system is used to collect the achromatic image corrected by the Schupmann scheme. The whole Schupmann compensation diffractive telescope system is presented in Fig. 1.

Note that the telescope system in Fig. 1 is fully illuminated by a multi-wavelength light (i.e., labelled red) covering the whole aperture. After passing through the primary DOE, the incident light is spread both physically and spectrally into different directions because of the chromatic aberration. Afterwards, the dispersed light is focused into a certain plane by a field lens introduced between the two DOEs. Here, the primary DOE and the secondary DOE are spatially conjugate with respect to this field lens. Moreover, the central wavelength light of the

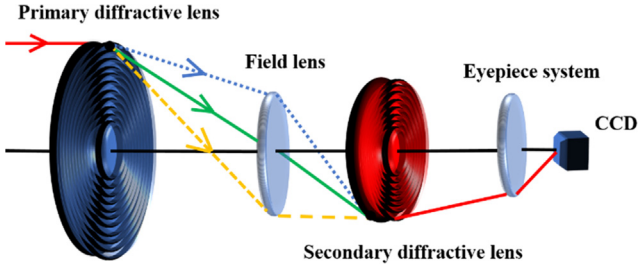

Fig. 1. Optical scheme of the Schupmann compensation diffractive telescope system.

telescope system (i.e., green line in Fig. 1) passes through the field lens center. At the front surface of the secondary DOE, all light is converged into a same image point corresponding to its object point on the primary diffractive lens, and the physical dispersion is corrected. On the other hand, the secondary DOE is feasible to eliminate the spectral dispersion generated by the primary DOE. At last, the spectrally corrected light is focused to the CCD by the eyepiece optical system. To more accurately study the imaging process, light propagation is numerically studied by using the optical transfer matrix as depicted by Hyde et al. [14]. The input light and the output light (light received by the CCD) are represented by two parameters (x,θ) with x represents the spatial position and θ represents the spatial direction in the meridional plane. The light is sequentially passing through the primary diffractive lens, the field lens, the secondary diffractive lens and the eyepiece system, so the corresponding optical transfer matrix equation is defined as Eq. (3) [14],

$$\begin{pmatrix} x_{out} \\ \theta_{out} \end{pmatrix} = \begin{bmatrix} 1 & L \\ 0 & 1 \end{bmatrix} \cdot \begin{bmatrix} E_{11} & E_{12} \\ E_{21} & E_{22} \end{bmatrix} \cdot \begin{bmatrix} 1 & 0 \\ -C(\lambda) & 1 \end{bmatrix} \cdot \begin{bmatrix} F_{11} & F_{12} \\ F_{21} & F_{22} \end{bmatrix} \cdot \begin{bmatrix} 1 & 0 \\ -D(\lambda) & 1 \end{bmatrix} \cdot \begin{pmatrix} x_{in} \\ \theta_{in} \end{pmatrix}. \tag{3}$$

On the right side of Eq. (3), the first matrix represents the light propagation from the eyepiece to the CCD with a propagation distance of L; the second and the fourth matrices E and F represent the optical modification introduced by the eyepiece system and the field lens. Here, these two elements are regarded as achromatic. The third and the fifth matrices, which contain the components dependent on the input light wavelength (i.e., $D(\lambda)$ and $C(\lambda)$), imply the spectral modulation ability of the primary diffractive lens (i.e., $D(\lambda)$) and the secondary diffractive lens (i.e., $C(\lambda)$), respectively.

The first and the second matrices in Eq. (3) are spectral independent. Hence, only the product from the third matrix to the fifth matrix will determine the spectral dispersion. The product of these three matrices M is shown in Eq. (4),

$$\begin{bmatrix} M_{11} & M_{12} \\ M_{21} & M_{22} \end{bmatrix} = \begin{bmatrix} F_{11} - D(\lambda)F_{12} & F_{12} \\ F_{21} - D(\lambda)F_{22} - C(\lambda)F_{11} + D(\lambda)C(\lambda)F_{12} & F_{22} - C(\lambda)F_{12} \end{bmatrix}. \tag{4}$$

To achieve spectral dispersion correction, each component in M should be wavelength independent, so all four contents in matrix M should be constants. This leads to a conclusion that F_{12} should be 0, and a further relation can be obtained as Eq. (5),

$$C(\lambda) = \frac{F_{21} - M_{21}}{F_{11}} - D(\lambda)\frac{F_{22}}{F_{11}}. \tag{5}$$

The chromatic independent term in Eq. (5) (i.e., $(F_{21} - M_{21})/F_{11}$) is directly incorporated into the further matrix calculation, and it will not cause any chromatic dispersion because the first and the second terms in Eq. (3) are also achromatic. Moreover, term F_{11} is the magnification (here we use α to demonstrate the magnification) of the primary diffractive lens with respect to the secondary DOE. At last, as F is an optical transfer matrix, it is commonly presented as a unit determinant. Therefore, as F_{12} is already 0, the product of F_{11} and F_{22} should equal to 1. At this moment, the relation between $D(\lambda)$ and $C(\lambda)$ in Eq. (5) can be further presented by Eq. (6) without considering the achromatic component as,

$$C(\lambda) = -\frac{D(\lambda)}{\alpha^2}. \tag{6}$$

Once we obtain Eq. (6), the spectral dispersion factors $D(\lambda)$ and $C(\lambda)$, which represent the light convergence ability of different wavelengths, are analogue to the optical power of the DOEs. Therefore, the focal length relation between two DOEs is described by Eq. (7),

$$f_p = -\alpha^2 f_s \tag{7}$$

where Eq. (7) is one sufficient condition to implement an achromatic diffractive telescope system. Here, f_p is the focal length of the primary DOE and f_s is the focal length of the secondary DOE. Moreover, both focal lengths are defined to the central wavelength. On the other hand, Schupmann theory demands the secondary DOE to provide a magnification of α. What is more, the secondary DOE should share a same amount of Fresnel ring as the primary DOE (i.e., both DOEs should have a same pattern). Hence, by using f_{number} of both DOEs as criteria, we obtain a secondary sufficient condition to perform the diffractive telescope system design as Eq. (8),

$$f^p_{number} = \alpha f^s_{number}. \tag{8}$$

We want to emphasize that Eqs. (7) and (8) are the ultimate telescope system design indications. Now, to achieve high-resolution imaging with a large f_{number}, as well to alleviate the secondary DOE fabrication difficulty, the magnification factor α should be selected as a small integer.

To implement a complete diffractive telescope system, the parameters of the field lens and the eyepiece optical system should also be obtained. Now, we select diameter D_p and focal length f_p of the primary DOE as the initial parameters. Hence, the diameter of the secondary DOE D_s and its focal length f_s can be determined with the help of Eqs. (7) and (8). Note that as the field lens is used to obtain the conjugate imaging of the two DOEs, the field lens has to be located at both the back focal plane of the primary DOE and the front focal plane of the secondary DOE with respect to the designed central wavelength. The focal length of the field lens f_f then can be determined as Eq. (9),

$$f_f = \frac{f_p}{1 + \alpha}. \tag{9}$$

The eyepiece system, which is used to focus the light from the secondary DOE corrector to the CCD, is considered as a thin lens. To ease the system calibration and to avoid the light loss, the primary surface of the eyepiece system is normally located close to the back surface of the secondary DOE corrector, or even these two elements are consolidated together to obtain a hybrid diffractive-refractive element [37].

2.2. Compact diffractive telescope by inserting a relay lens system

Even though a diffractive telescope can be designed achromatically by introducing Schupmann principle, the whole optical system sketch is long because we use a large f_{number} DOE as the primary lens. For instance, a DOE with a diameter of 300 mm and a f_{number} of 100 implies a whole telescope system length greater than 35 m. In this case, air turbulence will deteriorate the image quality dramatically. Under this scenario, a telescope compact method is proposed. Specifically, we implement a relay lens of great optical power between the primary diffractive lens and the field lens. By this mean, the imaging quality of the telescope system is not deteriorated and on the other hand, the system sketch is effectively compacted so that the air turbulence effect is eliminated.

The compact diffractive telescope has a similar scheme as the

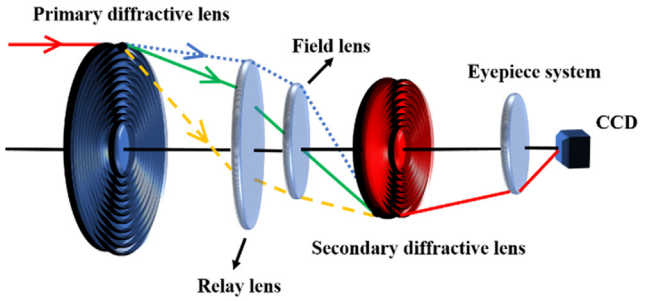

Fig. 2. Optical scheme of the compact Schupmann diffractive telescope system by inserting a relay lens.

original four-elements-contained diffractive telescope (i.e., the diffractive telescope scheme in Section 2.1), but a relay lens is added between the primary DOE and the field lens. The multi-wavelength incident light entering the primary DOE is firstly converged to different directions corresponding to each wavelength. Then, rather than being directly collected by the field lens, the light rays propagating through the primary DOE are converged by the relay lens so that a greater light convergence is obtained. Under this scenario, we acquire a better converged light at the front surface of the field lens. Therefore, the spatial length of the whole system sketch is compacted. The optical scheme of the compact diffractive telescope system is presented in Fig. 2. By locating this relay lens close to the backward surface of the primary diffractive lens, an effective system sketch compression is achieved, but the relay lens should have a great aperture. On the other hand, by locating the relay lens close to the field lens, we only need a relay lens of small aperture, which in fact is easy to be fabricated. However, by utilizing this second scheme, we cannot effectively compact the telescope system, because we can only compress the short distance from the relay lens to the DOE corrector.

To obtain chromatic aberration correction in this compacted diffractive telescope system, the parameters of the primary DOE and the secondary DOE should still satisfy Schupmann correction condition (i.e., Eqs. (7) and (8)). So, the image of the primary DOE via both the field lens and the relay lens should coincide with the front surface of the secondary corrector DOE. What is more, the central wavelength light ray should pass through the geometric center of the field lens. By considering the above restrictions, we can calculate the relay lens parameters. In particular, the focal length of the relay lens f_r and its distance to the field lens d_{rf} should be determined. Note that as the relay lens is inserted between the primary DOE and the field lens, we can calculate the focal length of the relay lens as Eq. (10) with two given distances as: (*i*) the distance from the primary DOE to the relay lens d_{pr}, and (*ii*) the distance from the field lens to the secondary DOE d_{fs}. Moreover, α is the magnification of the primary DOE compared to the secondary DOE, and f_p is the focal length of the primary DOE with respect to the central wavelength,

$$f_r = \frac{\alpha \cdot d_{fs} \cdot (f_p - d_{pr})}{f_p - \alpha \cdot d_{fs}}. \tag{10}$$

Once the focal length of the relay lens is determined, the distance from the relay lens to the field lens can be consequently calculated as Eq. (11),

$$d_{rf} = \frac{(f_p - d_{pr}) \cdot f_r}{f_r + f_p - d_{pr}}. \tag{11}$$

Finally, we want to emphasize that the above-discussed designing indications could be used to instruct the initial structure design of a diffractive optical telescope. Nevertheless, to perform a final telescope design with considering the optical aberration correction, ray-tracing software such as Zemax or CODE-V should be used to accomplish the system optimization.

3. Implementation of large aperture diffractive optical lens (DOE)

In Section 2, we have proved that a large diameter primary DOE and its inversed correction DOE are the fundamentals to implement a large aperture diffractive telescope. Therefore, in this section, we mainly discuss the techniques to obtain diffractive optical elements. Specifically, we firstly elucidate the usage of optical lithography technique to fabricate both phase-modulated and amplitude-modulated DOEs. In particular, we discuss two types of DOE as Fresnel zone plate (FZP) and photon sieve. Afterwards, we present thin membrane DOEs as such elements are more flexible. Finally, we demonstrate subaperture DOE stitching technique, which is mandatory to implement a large aperture diffractive telescope.

Diffractive optical element (DOE) is an optical element with periodically distributed microstructures (i.e., ring structures) fabricated on its surface. To fabricate certain microstructures on its surface, two major techniques are utilized as: (*i*) single-point diamond turning [38-40] and (*ii*) optical lithography [41,42]. Single-point diamond turning can fabricate DOE patterns with a high precision three-dimensional displacement platform. Unfortunately, this technique is not advisable for some materials such as fused silica, because surface damage is extensively responsive to the diamond grit size [43]. What is more, single-point diamond turning technique is precision limited for an insignificant linewidth [44]. Under this scenario, optical lithography techniques [45] are commonly applied such as laser direct writing [46–48], UV lithography [49–51], electron beam lithography [52,53] and ion beam lithography [54–56]. Laser direct writing uses a spatial controllable laser focal spot to form the shape of the desired microstructure outline. This method can provide ultra-high precision, but its efficiency is low. Deep UV lithography use an ultra-violet beam as the light source to illuminate the photolithography masks to transfer the patterns to the wafer. This technique can efficiently fabricate the whole structure with just one exposure, but its precision is greatly influenced by the aberration of the projection objective lens. Ion beam lithography and electron beam lithography share the same principle configuration with only the light sources divided as ion beam or electron beam. In fact, ion beam lithography is more widely used because of their stable performance. By using electron beam or ion particle beam, the resolution can be enormously enhanced at the price of low efficiency and high cost.

3.1. Phase-modulated DOE fabrication

Phase-modulated DOEs are able to modulate the phase of the propagated light with its surface microstructures, and thus, we can obtain the desired wavefront. The most commonly used phase-modulated DOEs in a diffractive telescope system are Fresnel zone plates (FZPs) or photon sieves. Specifically, they act as the primary diffractive lens and the secondary corrector lens.

3.1.1. Phase-modulated FZP fabrication

A phase-modulated FZP has periodically distributed rings, and the rings have different heights. To be more specific, the height distribution in any ring contains L-level from which a “stair” structure is formed. Moreover, a whole L-level “stair” provides a phase modulation as 2π. In our case, the focal length of the FZP can be calculated by Eq. (1), and the width of each ring can be obtained by Eq. (12),

$$w_F = \frac{f\lambda}{D_F}, \tag{12}$$

where f is the focal length of the FZP, λ is the wavelength of the incident light and D_F is the diameter of any ring. The height of each level in one particular ring contributes a phase modulation of $2\pi/L$, so the height of each level is represented by Eq. (13),

$$h = \frac{(L-1)\lambda}{L(n-1)}, \tag{13}$$

where n is the substrate refractive index.

As a DOE generally has a great focal length, we can tell from Eq. (12) that the width of any ring in a regular FZP is greater than the input wavelength, and this makes UV lithography a suitable method to fabricate FZPs. Here, in order to fabricate a multi-level FZP, we can introduce a consecutive lithography process which only requires one photolithography mask [57].

Apart from optical lithography, maskless laser direct writing is another useful tool to fabricate multi-level DOE. In laser direct writing, we initially coat the substrate with photoresist material before laser exposure. Then, we use a high numerical aperture (NA) objective lens to focus the laser into a focal spot, and we control the spatial position between this laser spot and the substrate to form the FZP pattern by optical exposure [58,59]. Finally, FZP patterns can be transferred to the substrate by performing the development to the exposed photoresist material [45]. In the real implementation, large aperture FZPs had been fabricated by rotating the substrate and by radially moving the objective [60,61].

3.1.2. Phase-modulated photon sieve fabrication

In the above section, we have presented the fabrication of a phase-modulated FZP. Nevertheless, high order diffraction and scattering will deteriorate the FZP imaging performance. Therefore, photon sieves are introduced into diffractive telescope systems, because they are suitable to both eliminate high order diffraction and suppress scattering [62,63]. Moreover, by implementing wavefront coding, the chromatic aberration of the photon sieve can be corrected, so that we can achieve broadband imaging [64-66].

Photon sieve is one particular kind of Fresnel zone plate that any FZP rings are filled with circular pinholes. One example of a photon sieve is shown in Fig. 3. Here, light passing through the small pinholes in the photon sieve is converged into its focal point by diffraction. Hence, the focal length and the ring width of a photon sieve can be calculated by Eqs. (1) and (12), respectively. Moreover, the contribution of any pinhole to the total intensity on the focal point can be determined by Eq. (14) as an oscillating function,

$$F \propto \frac{d}{w} J_1\left(\frac{\pi d}{2w}\right), \tag{14}$$

where J_1 refers to Bessel function, w and d are the FZP zone width and the pinhole diameter, respectively [26]. If F is positive, we have the intensity enhanced at the focal point, and vice versa, a negative F contributes to a decreased focal intensity. Here, we want to emphasize that in the real design, the pinhole diameter can be enlarged beyond its corresponding ring width. In fact, to ensure a best focalization, the ratio d/w in Eq. (14) is set at 1.53 (or 3.53, 5.53 et al.) which provides an optimal condition for Bessel function. Moreover, the enlargement of the pinhole diameter can ease the fabrication difficulty because a large diameter pinhole is easy to be fabricated. Furthermore, the pinholes can be distributed either randomly or regularly only if they are not overlapped. In fact, pinhole distribution mainly determines the optical throughput which will influence the final photon sieve efficiency.

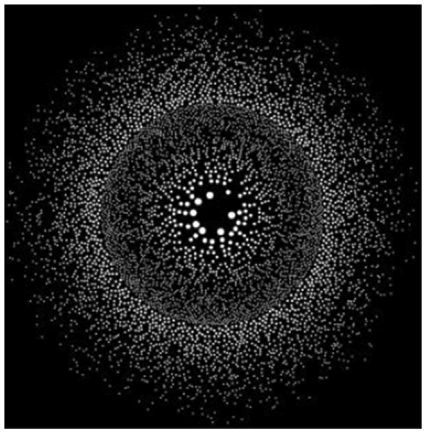

Fig. 3. Pinhole distribution of a photon sieve [75].

For phase-modulated photon sieve, pinholes are fabricated on a transparent substrate with each pinhole has a certain depth. Later, the wavefront is modulated by these pinholes, so the incident light is converged to the focal plane. In order to fabricate phase-modulated photon sieves, we still introduce either UV lithography or laser direct writing. These two fabrication processes are similar to those used in FZP fabrication.

On the other hand, recent study about photon sieves demonstrates that laser ablation technique is also available for photon sieve fabrication [67,68]. To be more specific, Julian et al. had fabricated holes of a photon sieve by directly ablating the polyimide substrate with a laser spot. In their scheme, the diameter of the laser spot is around 15 μm. As a result, a 19-ring distributed binary photon sieve with its focal length as 400 mm is obtained, and it demonstrates a diffraction efficiency of 11% [67,68].

3.2. Amplitude-modulated DOE fabrication

In Section 3.1, we mainly discuss phase-modulated DOEs. Nevertheless, amplitude-modulated DOEs are also widely used in diffractive telescope systems especially for ultra-short wavelength imaging. Therefore, it is mandatory to study amplitude-modulated DOE fabrication. In fact, amplitude-modulated DOEs share a same ring pattern or pinhole pattern as phase-modulated DOEs, but they modulate the wavefront by blocking a certain portion of the incident light with the non-transparent sections but transmitting the remaining light. Under this scenario, any ring width for an amplitude-modulated DOE is equal to a phase-determined DOE if these two DOEs have the same diameter and focal length.

3.2.1. Amplitude-modulated FZP fabrication

Differ from a phase-determined FZP, an amplitude-modulated FZP contains both opaque and transmissive rings consecutively distributed on the substrate. Moreover, the indispensable “stair” structures in a phase-modulated FZP do not exist in an amplitude FZP. On the contrary, all rings are located in the same plane (i.e., the substrate plane). Under this scenario, we can fabricate the amplitude-modulated FZP by using the same UV lithography or laser direct writing technique. In general, three steps should be performed. First of all, we coat the substrate (i.e., glass or silica) with a thin layer of opaque material which is etching friendly. Next, we use either UV lithography or laser direct writing to transfer the ring pattern to the substrate. Finally, by performing photolithography development and then ion beam etching with precisely controlled etching time, we can get the consecutive opaque-transmissive ring pattern.

It should be noted that amplitude-modulated FZPs provide a weaker diffraction efficiency compared to phase-modulated FZPs with the same aperture and focal length. Therefore, amplitude-modulated FZP is more widely applied in ultra-short wavelength imaging diffractive telescope system.

3.2.2. Amplitude-modulated photon sieve fabrication

The basic scheme of a photon sieve is previously depicted in Section 3.1.2 (see Fig. 3). It is one kind of FZP with homogenously distributed holes on each ring. While the phase-modulated photon sieve modulates the wavefront by transmitting all the light, the amplitude-modulated photon sieve, on the other hand, only allows the light to go through the transmissive pinholes. Compared to phase-modulated photon sieves, amplitude-modulated photon sieves have a weaker diffraction efficiency. For instance, the electroformed nickel photon sieve or the diazo polymer photon sieve fabricated by Anderson [26] only provides a diffraction efficiency of 0.4% and 0.34%, respectively. Even though

they present weak diffraction efficiency, the amplitude-modulated photon sieves are those being most commonly investigated in diffractive telescope systems at present. This is because amplitude-modulated photon sieves are flexible to be fabricated on a thin polyimide membrane, which shows its benefit to be used as the primary lens in a light-weight telescope (see Section 3.3).

To obtain the amplitude-determined photon sieve, the same UV lithography or laser direct writing method above discussed can be directly applied. However, photon sieves contain a great number of holes, this means the photolithography mask fabrication is complicated. Thus, laser direct writing is more suitable to fabricate amplitude-modulated photon sieves, because we can avoid preparing the complicated photolithography mask and therefore the fabrication efficiency can be enhanced.

3.3. Membrane diffractive optical element

The above-discussed two sections present the methods to obtain either amplitude or phase-modulated diffractive optical elements (i.e., Fresnel zone plates or photon sieves). Unfortunately, all above-mentioned DOEs are fabricate on either silica or glass. Note that these materials are bulky to be implemented in space diffractive telescopes. Therefore, we demonstrate in this section the superiority of utilizing a thin membrane to replace a regular thick substrate for DOE fabrication, and we also present the challenges in utilizing such membrane DOEs.

Note that large aperture diffractive telescopes are investigated to be eventually applied for space mission. Therefore, the telescope weight as well its structure has to be carefully considered to satisfy the launching requirement. For silica based FZPs, even though they can be used to perform high quality imaging, they have a relatively large weight (~4 kg/m^2) compare to the thin film membrane (~0.5 kg/m^2), and this makes silica FZPs more costive for space mission [69]. Moreover, membrane is more flexible than thick silica, so we can also use membrane DOE to ease the launching difficulty [70–72]. Under this scenario, thin film membrane DOEs were investigated and then tested by using different membrane material. For instance, Novastrat thin film membrane (Nexolve Corp.) demonstrates great advantage compared to other thin films for its great non-zero thermal expansion coefficient (50 ppm/°C to −10 ppm/°C) [69]. Once the membrane is determined, any DOE pattern (i.e., FZP rings or photon sieve pinholes) can be printed on the membrane by using either lithography or laser direct writing we discussed in Sections 3.1 or 3.2. However, due to the physical fragile characteristic of the thin membrane, several challenges are inevitable during the membrane DOE fabrication, such as: (*i*) the membrane dimensional instability and (*ii*) the manufacturing load [73]. For the first issue, membrane dimensional instability introduces surface wrinkle, and this leads to DOE pattern fabrication error. Therefore, a membrane holding frame is mandatory to conjoin the whole membrane to the frame boundary so that we can ensure a surface free of wrinkle. Specifically, among numerous holding frames, the circular, the square and the trapezoidal schemes present great performance and they are shown in Fig. 4. Next, for the manufacturing load issue, we want to note that the already conjoined membrane has to be cut into expected shapes in most cases to satisfy different applications. Therefore, the residual force introduced during the cut will be again inevitably added into the new membrane, thus the membrane surface will be wrinkled. To solve this surface wrinkle introduced by the manufacturing load, we have to study the internal force distribution at the boundary of the whole newly cut membrane, and we should guarantee the joint force of any node in the new membrane to be balanced (the joint force should be zero). However, we limit our discussion on membrane manufacturing load in this review, and we only give one example in Fig. 5. Here, we show in Fig. 5 the force distributions on the original membrane (i.e., yellow section) and the cut membrane (i.e., blue section).

Apart from the two above-mentioned fabrication challenges, one major difficulty in using the membrane DOEs especially for space

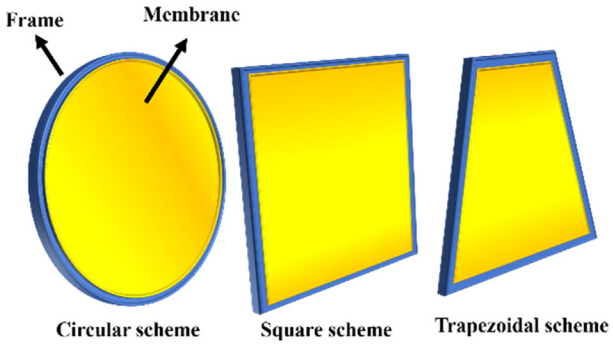

Fig. 4. Membrane conjoining schemes by using different holding frames.

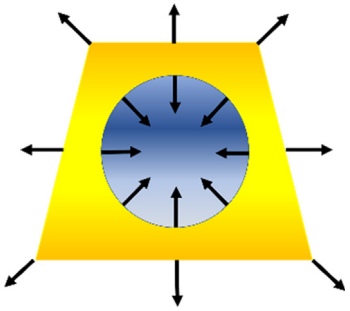

Fig. 5. The boundary loads of the original membrane (yellow section) and the cut membrane (blue section). (For interpretation of the references to colour in this figure legend, the reader is referred to the web version of this article.)

mission is the membrane acoustic load [73]. We want to emphasize that for the membrane, its stiffness matrix is not a constant, but it is varying as a result of different pressure levels. Now, let us consider that the pressure is randomly generated by the acoustic energy introduced by random blasts during the launch. As a consequence, such acoustic energy will deform the membrane DOE surface shape. Hence, to maintain the performance of the membrane DOE, the surface deformation implemented by the acoustic pressure has to be compensated. One possible method to accomplish the surface compensation is to acquire the real launching data to engage numerous simulations for the membrane surface deformation as a function of different pressures. Afterwards, we can inversely compensate the deformed membrane DOE.

3.4. Subaperture stitching Fresnel diffractive elements

A large diameter primary lens is mandatory to realize high-resolution imaging in a diffractive telescope. Nevertheless, either optical lithography or laser direct writing technique is not feasible to directly fabricate an ultra-large aperture DOE. For lithography, a large-scale photolithography mask is very difficult to obtain, and a uniform UV illumination fully covering the fabricated substrate to perform lithography exposure is practically unachievable. For laser direct writing, it is difficult to accurately control the laser writing precision at a large scale. Under this scenario, it is of great interest to study subaperture stitching DOE. Even though subaperture stitching principle is enormously studied for reflective mirrors [9,10], subaperture stitching DOEs are rarely reported. Domber et al. firstly proposed a 6 subapertures stitched membrane DOE applied in a diffractive telescope system [28,29]. In their system, the designed diameter of the primary FZP is 5 m, and the whole piece is a 45° segmented fragmentary aperture. Afterwards, Yan et al. studied the subaperture stitching principle by implementing a fully covered four-squares-sectored photon sieve of 100 mm diameter [74]. Nevertheless, they only qualitatively analysed the stitching error in one dimension. Until recently, Zhang et al. [31] proposed a universal subaperture stitching error study by

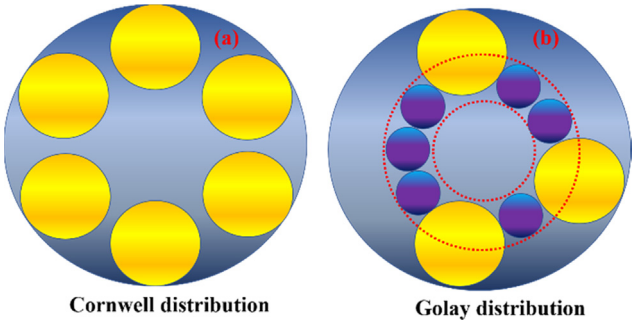

Fig. 6. Suabaperture layouts: (a) Cornwell distribution and (b) Golay distribution.

completely considering the DOE stitching error in five degrees of freedom.

Like the subaperture stitching reflective mirrors, the subaperture layout of a DOE also shares the general layout such as Cornwell layout [75] or Golay layout [76] (see Fig. 6). Note that even though the subapertures presented in Fig. 6 are circle pieces, they can be arranged to other shapes such as square or trapezoid. Here, Cornwell distribution guarantees that the same diameter subapertures can be uniformly distributed in the same ring. On the other hand, Golay distribution requires the number of the subapertures in each ring being an integer multiple of 3. In fact, Golay distribution can provide a higher filling factor by taking benefit of different subaperture sizes. Even though different layouts influence the imaging quality diversely, the subaperture stitching principle can always be elucidated within any subaperture shape by the means of optical path difference [31]. For instance, we present a certain piece B' in a Cornwell distributed subaperture DOE in Fig. 7, and this piece contains three types of error as radial offset error, axial offset error and radial rotating error.

Note that the DOE in Fig. 7 consists four subapertures where only B′ piece (yellow circle) is deviated from its ideal position (shadow gray circle at B) while the other three are suited in the correct positions. Here, B′ piece is situated away from the DOE plane and it demonstrates the axial offset error in X axis direction. Moreover, the projection of B′ piece on the DOE plane does not coincide with its ideal position, but it is displaced for a certain distance in either Y or Z axis direction, this is regarded as the radial offset error. Finally, it is obvious that B′ is rotated for a certain angle from the DOE plane from which we can tell the radial rotating error. The subaperture stitching error tolerances of the three above-mentioned errors can be studied by calculating the optical path differences, respectively.

At this moment, we consider this circle subaperture and analyse its stitching error tolerance. We initially study the radial offset error and we assume the subaperture is displaced for a distance Δr. This is represented in Fig. 8, where the blue piece means the subaperture is at its ideal position, and the red piece means the subaperture is displaced.

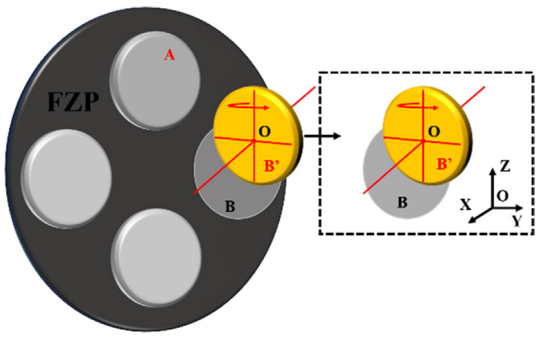

Fig. 7. Cornwell distributed subaperture DOE with B' piece showing radial offset error, axial offset error and radial rotating error.

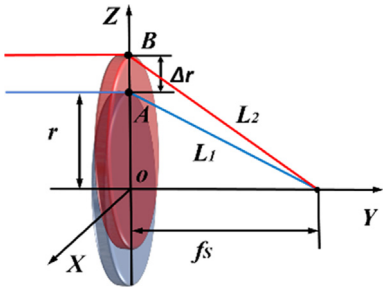

Fig. 8. Subaperture radial offset error configuration.

The focal length of the subaperture is f_s and its radius is r. Then, we calculate the optical paths from the subaperture outermost position to the focal length, we obtain two optical paths as L_1 and L_2. Finally, by considering that these two optical path differences should follow the Rayleigh criteria as $\lambda/10$, we obtain the subaperture stitching radial error tolerance as [31],

$$\Delta r = \frac{\lambda f_s}{10r}, \tag{15}$$

where λ is the wavelength of the input illumination.

The axial displacement case is also investigated using the same circle subaperture, but it presents an axial offset of Δy. The axial offset configuration is given in Fig. 9 with a supplementary angle $\theta(r)$ determined by both the original optical path L_1 and the modified optical path L_2.

Then, by again calculating the optical path difference between L_1 and L_2, we obtain the axial offset error tolerance by using Rayleigh criteria as [31],

$$\Delta y = \frac{\lambda f_s}{5r^2}. \tag{16}$$

Finally, the radial rotating error scheme is shown in Fig. 10 by rotating the subaperture of an angle θ around the circle geometric center. Again, by calculating the optical path difference and introduce Rayleigh criteria, we obtain the radial rotating error tolerance as [31],

$$\Delta\theta = \frac{\sqrt{6.4\lambda (f_{number})^3 + r} - \sqrt{r}}{4f_{number}\sqrt{r}}, \tag{17}$$

where f_{number} is the f-number of the subaperture piece.

To verify the above-proposed stitching error tolerance theory, a three-belt subaperture stitching FZP is implemented. This amplitude-modulated FZP has 529 rings and its diameter is 300 mm. The inner belt subaperture A is a circle with the radius of 39.96 mm, the second ring B has a width of 28.70 mm while its ring center coincides with the circle center of A piece, and the outermost subaperture ring C has a width of 37.88 mm. What is more, the distance from the outermost edge of A piece to the inner edge of B piece is reserved as 20.10 mm to install the displacement adjusting device for subaperture shifting, and the outermost edge of B subaperture is designed 23.35 mm away from the inner

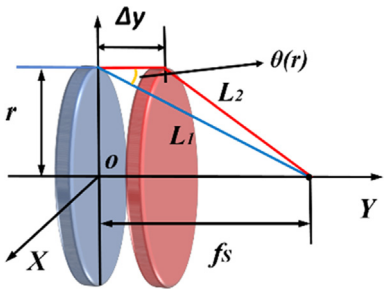

Fig. 9. Subaperture axial offset error configuration.

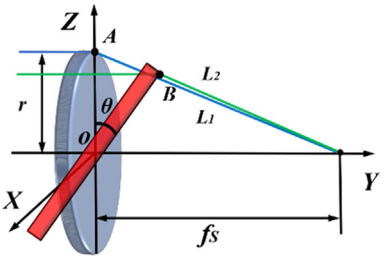

Fig. 10. Subaperture radial offset error configuration.

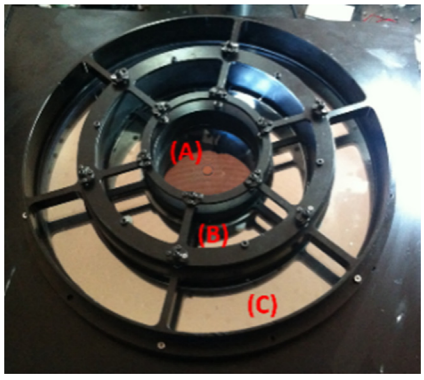

Fig. 11. Configuration of a 300 mm diameter three-ring distributed subaperture stitching FZP.

edge of C piece. The configuration of the three-belt subaperture stitching FZP is given in Fig. 11.

The theoretical error tolerances of the subaperture FZP described in Fig. 11 can be calculated with the above-provided equations (i.e., Eqs. (15)–(17)). Here, we only select C belt to analyse the error tolerance. By theoretically calculating the error tolerance of C belt, its corresponding radial error tolerance is 12.656 μm, the axial error tolerance is 5.062 mm and the rotation error tolerance is 0.08°. Afterwards, we also implement the Zemax simulation, it is clearly demonstrated that the simulation results agree with the theoretical calculation results. The comparison of the simulation results and the theoretical calculated results are given in Table. 1. What is more, to demonstrate the imaging quality of the FZP presented in Fig. 11, we also simulate the point spread function (PSF) of this subaperture stitching DOE, and its PSF pattern is given in Fig. 12. The simulated SFP pattern agrees with the experimental measurement result presented in Ref. [31].

Finally, we also experimentally verify the stitching error tolerance theory by measuring the resolution board of this subaperture DOE. Specifically, we spatially displace C belt along the axial direction for 5 mm, and the maximum signal frequency was measured as 3.57 cy/mm. Moreover, the maximum signal frequency was measured as 3.79 cy/mm without any DOE stitching error. The above demonstrated resolution testing results agree with the theoretical stitching error analysis, and thus, it demonstrates the correctness of the optical path difference-based stitching error theory proposed by Zhang et al. [31].

Table 1
The theoretical error tolerances and the simulation results of the C belt subaperture.

Error type	Radial offset	Axial offset	Rotation
Theoretical results	12.656 μm	5.062 mm	0.08°
Simulation results	12.66 μm	5.06 mm	0.08°

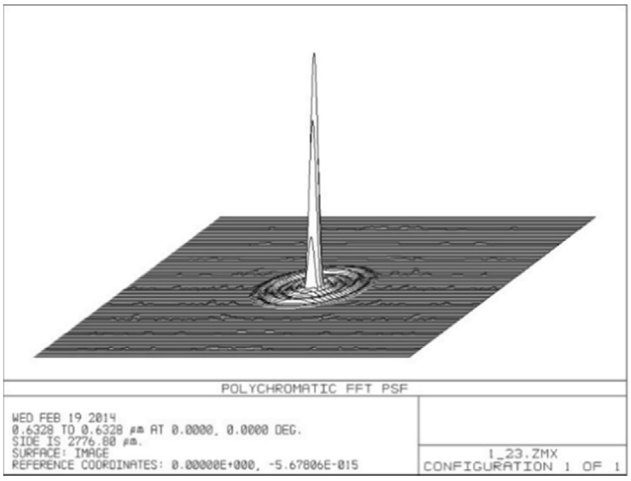

Fig. 12. Simulated point spread function (PSF) pattern of the three-belt subaperture stitching DOE.

4. Experimentally implemented large aperture diffractive telescope systems

So far, the optical design principle for large aperture diffractive telescopes is thoroughly discussed (see Section 2), and the DOE fabrication methods as well as the subaperture stitching theory are depicted (see Section 3). Therefore, to investigate the imaging ability of diffractive telescope systems, the telescopes must be experimentally implemented and tested. In this section, we illustrate different diffractive telescopes specialized for different applications. In particular, we review five kinds of large aperture diffractive telescopes from different perspectives.

4.1. FZP based large aperture diffractive telescope

The concept of FZP based Schupmann correction diffractive telescopes was firstly proposed by Hyde et al. as Eyeglass [14,16]. Such system later became the prototype scheme for any broadband diffractive telescope which consists two separated sections as: (*i*) a large aperture diffractive lens as the primary lens and (*ii*) a chromatic corrector contained eyepiece. By applying this scheme, Hyde et al. implemented two diffractive telescope systems with the diameters as 20 cm and 50 cm, respectively. The 20 cm diameter DOE employed in the first telescope was a 4-level phase-modulated element with a f_{number} of 100, while the chromatic corrector has a diameter of 2.2 cm and its f_{number} of 11. We want to note that these parameters satisfy the system design indications depicted by Eqs. (7) and (8). Finally, both the imaging quality and the chromatic aberration correction ability of this telescope were validated by testing the diffraction limited images with broad-band light (470–700 nm) and by imaging the real astronomy object. On the other hand, the second 50 *cm* diameter telescope was implemented by using a silica binary DOE with its f_{number} as 100. However, this larger diameter diffractive telescope requires a great system sketch, and thus both a robust system calibration and a sophisticated eyepiece system design are mandatory.

Apart from the Hyde systems which are validate in the visible light range, Koechlin et al. also studied the Fresnel lens based diffractive telescopes which mainly focus on either the near infrared or the ultraviolet light domain [20–23,77–84]. First, they implemented a 200 mm aperture diffractive telescope by using square FZP (i.e., “Gen II”). Specifically, Gen II works at two spectral bands as visible light range (630–745 nm) and near IR range (750–790 nm). The sketch of Gen II diffractive telescope is shown in Fig. 13 where the primary DOE and the eyepiece are implemented on a 19 m long tube [21].

Gen II telescope can provide a dynamic range greater than 10^{-5} and

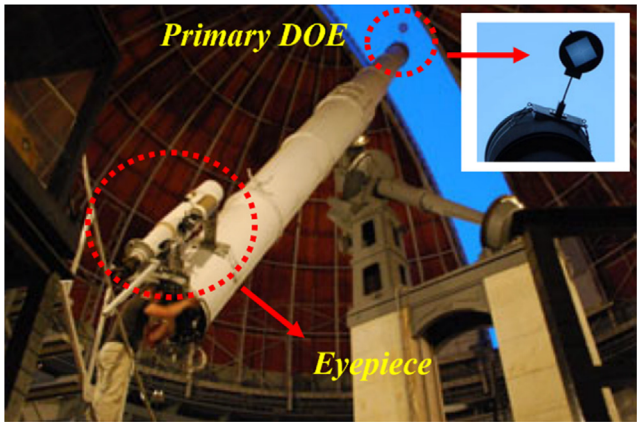

Fig. 13. Scheme of the "Gen II" diffractive telescope [21].

a resolution of 0.8″ at 800 nm, but the field of view (FOV) is limited to about 500″ because of the finite size of the field lens optics [20]. In fact, the telescope FOV must be compromised if a wide spectral bandpass is desired. This can be demonstrated by Eq. (18) [78],

$$\frac{\Delta\lambda}{\lambda} = \frac{2\cdot D_f - 1.22\cdot n\cdot\frac{D_p}{8N}}{D_p}, \tag{18}$$

where the left term is the spectral bandpass in the zero unvignetted field. On the right side, n is the FOV diameter in the number of resolution elements (i.e., the resolution element has an angular extension of $1.41\lambda/D_p$ for a square pupil of diagonal D_p, and $1.22\lambda/D_p$ for a circular pupil of diameter D_p), N is the FZP zone number, D_f and D_p are the diameters of the field optics and the FZP, respectively. Indeed, even though a large FOV guarantees a wide spectral bandpass implied by Eq. (18), the intensity entering the telescope will be dramatically reduced because of the optical vignetting. Hence, the imaging quality of the wide spectral bandpass telescope is decreased by a large FOV and therefore a compromise between the FOV and the spectral bandpass must be considered before the system design.

Soon after, Koechlin et al. also proposed a second diffractive telescope (Fresnel Imager) dedicated to UV astronomy observation at the wavelength around 260 nm [22]. The 65 mm aperture primary FZP is fabricated on a fused silica plate with the focal length designed as 12.7 m at the central wavelength, the chromatic aberration correction ability of this telescope was validated by imaging the USAF targets [22]. We want to highlight that such diffractive telescope has one major advantage compared to the regular reflective telescopes in UV wavelength domain because the UV light can be easily focused by the transmissive FZP without losing the high image contrast, and thus, the high imaging quality can be maintained. In fact, such characteristic makes FZP based large aperture diffractive telescopes an ideal optical instrument to fulfil space observation especially in the UV domain. Later, Koechlin also proposed the idea of a 15 cm aperture UV Fresnel Imager prototype (wavelength range from 120 nm to 200 nm) to be calibrated to the International Space Station with a total system length about 45 m in the future [23].

Finally, we want to note that such two-section based diffractive telescopes are still being broadly studied nowadays to achieve image quality enhancement [85,86]. In particular, the image quality can be improved either by suppress the system stray light [87] or by correct the optical aberration [88].

4.2. Photon sieve based diffractive telescope

We can deduce from the above section that the primary apertures of the wide spectrum imaging diffractive telescopes are mainly fabricated on silica substrate. Nevertheless, silica DOE based telescopes cannot meet some requirements such as extremely light weight for space mission or ultra UV imaging. This is because the silica is heavy, and its UV transmission is low. Under this scenario, the concept of using photon sieves in diffractive telescopes was proposed and membrane photon sieve telescopes were implemented.

As it is discussed in Section 3, photon sieve is one kind of FZP that its rings are replaced by the appropriately distributed circular pinholes. Under this scenario, Anderson et al. discussed the feasibility to manufacture the photon sieve pattern on the polymer membrane [26]. In fact, the membrane photon sieve can be fabricated by using lithography technology, which is similar to the regular silica-based DOE fabrication. Hence, the membrane thickness uniformity, the thermal property and the deployed flatness are the three major elements influencing the membrane photon sieves fabrication. Fortunately, it is possible to obtain proper membrane thickness uniformity and great thermal characteristic even though they are challenging, and more important, the surface flatness requirement of a membrane is much looser comparing to a traditional reflective mirror [16].

The first photon sieve telescope was proposed by Anderson et al. Specifically, this telescope uses a 0.1 m diameter, quartz plate based antihole photon sieve as the primary aperture, and the telescope imaging bandwidth is 40 nm (522–562 nm) [25]. Differ from a regular photon sieve, this antihole telescope allows the pinholes in the photon sieve to occupy the opaque Fresnel zone if any hole is not overlapped. Moreover, to fulfil the broadband imaging, the telescope system was designed by following the Schupmann chromatic aberration correction principle. Here, the primary aperture was the antihole photon sieve, and the chromatic corrector eyepiece was designed by introducing a reflection-refraction system. Finally, the system was tested by using an interferogram at two wavelengths (514.5 nm and 532.1 nm), and the testing results show closely similar Strehl ratios as 0.88 and 0.83, respectively. We can then deduce from these testing results that this photon sieve telescope is able to perform wide broadband imaging.

To further investigate the characteristic of a photon sieve telescope for space mission, Anderson et al. also proposed a similar structure diffractive telescope (i.e., FALCONSAT-7) by using a membrane photon sieve (Novastrat, provided by Nexolve) as the primary aperture [84,85]. For this zero-CTE polyimide membrane, it has a diameter of 20 cm and a thickness of 25 μm. The photon sieve partially presented in Fig. 14 has 2.45 million holes and its focal length operating at 654.45 nm is 40 m. Specifically, to obtain the photon sieve pattern, a contact printing technique was applied, and the pattern was finally etched on the membrane. Once the membrane photon sieve is obtained, the FALCONSAT-7 telescope system structure is subsequently implemented. Here the membrane photon sieve can be rolled inside a three-side spring-loaded pantograph which will be deployed once the telescope is launched into the space. On the other hand, the eyepiece optics is calibrated in a telescope optical platform shown in Fig. 15 [89]. Finally, we want to note that FALCONSAT-7 was designed for space mission with the

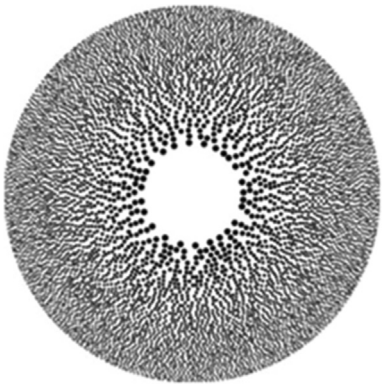

Fig. 14. Scheme of the photon sieve central section [25].

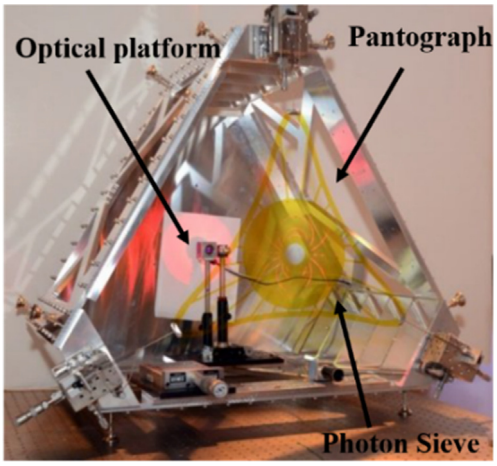

Fig. 15. Scheme of FALCONSAT-7 diffractive telescope system [89].

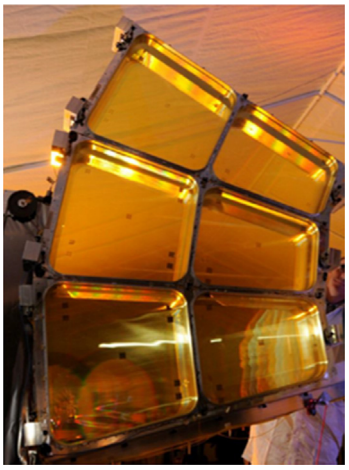

Fig. 16. 45° segmented trapezoidal subaperture stitching membrane DOE [29].

central wavelength at 654.45 nm and the FOV as 0.01° with an angular resolution of 4 μrad [15,90,91].

4.3. Subaperture stitching diffractive telescope

Note that both FZP based diffractive telescopes and photon sieve telescopes can satisfy a broad bandwidth imaging in a narrow field of view. Moreover, to achieve high-resolution imaging, a meter size class primary diffractive lens is compulsory. Unfortunately, it is extremely difficult to fabricate a meter scale DOE by optical lithography or laser direct writing. This fabrication restriction is mainly attributed to two aspects as: (*i*) the DOE surface defect such as DOE surface unflatness [92–94] and (*ii*) the imperfect fabrication process such as illumination nonuniformity [95,96] and optical distortion [97] during lithography exposure, or ion beam etching inhomogeneity [98]. Therefore, the concept depicted as fabricating small size subaperture DOEs and later stitch them together to forge a complete large-scale DOE is proposed. The subaperture stitching DOE process is explained as below. First, we design a complete large aperture DOE and determine its basic scheme. Afterwards, this complete DOE is separated into small, easy to build sections by using specific subaperture layout such as Cornwell layout or Golay layout. Here, it should be noted that circular, square and trapezoidal schemes are preferred to build any subaperture. Finally, each subaperture is separately fabricated and stitched together by locating them into the designed position. The above-mentioned subaperture stitching process is available for both subaperture stitching FZPs and photon sieves.

The first subaperture stitching DOE was proposed by Early et al. that they fully assembled a 75 cm diameter glass FZP with six circular sectors [29]. In this way, the focal spot of the precisely stitched DOE was measured as its diameter is nearly 50 μm, and this coincides with the theoretical result of 60 μm. The measurement result demonstrates that subaperture stitching is valid to obtain a meter size class DOE. Moreover, they also assembled a 5 m diameter, 250 m focal length foldable Fresnel lens with triangle and rectangular subapertures [70]. However, this subaperture DOE was not implemented in a diffractive telescope. On the other hand, Jin et al. suggested a four-piece, square shape subaperture stitching photon sieve [74]. The stitching process was simulated by only considering a two-dimensional error, and they proved that it is more critical to stitch the outer photon sieve subapertures rather than the inner ones.

The above-mentioned studies only focus on subaperture DOE characteristics, but these subaperture stitching DOEs have not been implemented into any telescope system. The first subaperture stitching DOE based diffractive telescope was proposed by Atcheson et al. as MOIRE telescope. The primary aperture of MOIRE is a 45° segmented trapezoidal membrane subaperture DOE of an aperture of 5 m. The subaperture stitching membrane DOE is shown in Fig. 16 [29]. Here, these subapertures are fabricated as trapezoidal, but in fact circle subapertures can promise a better uniform stress to reduce the membrane wrinkle [99]. To implement the diffractive telescope, the subapertures based primary lens (see Fig. 16) is installed to an aluminium frame and the eyepiece optics are located 27 m from this primary lens. The telescope system was implemented on a vibration free stage and it was later tested. First, this diffractive telescope was tested by simultaneously illuminating multiple subapertures in the primary DOE and the result demonstrates a NIIRS value below 3.5, which cannot meet the desired criterion (NIIRS of 3.5). Later, to better study the system performance, the telescope was tested by only illuminating one single subaperture, the NIIRS value at this moment is 2.3, which is weaker than the theoretically expected NIIRS value of 2.8 [29]. Note that the image quality decrease is mainly attributed to either the imperfect temperature condition or the air turbulence introduced by the long telescope sketch.

The above presented subaperture diffractive telescope proposed by Atcheson et al. does not have a full aperture. The primary lens is in fact a sectorial subaperture and it is not fully covering the whole aperture. Hence, Zhang et al. proposed a full aperture, three-belt distributed subaperture stitching diffractive telescope in which the primary lens is above depicted in Fig. 11 [31]. Moreover, the subaperture stitching error theory demonstrated in Section 3.3 was also applied to characterize the subaperture diffractive telescope performance. In this case, the telescope has a primary aperture of 300 mm and a total optical length of 35.49 m. The working wavelength is from 582 nm to 682 nm, the telescope focal length is 2000 mm, and the FOV is 0.15°. The photograph of this diffractive telescope is given in Fig. 17, and it is given from two perspectives for the sake of clarity. Here, we need to

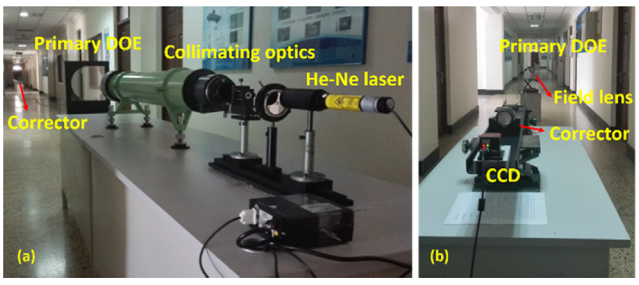

Fig. 17. The subaperture stitching diffractive telescope from: (a) the front perspective, and (b) the backward perspective. The whole telescope system contains a He-Ne laser, the collimating system, the primary DOE, the field lens, the chromatic aberration corrector and a CCD [31].

clarify that the primary DOE presented in Fig. 17 is in fact not presented as a stitching DOE, but in the real implementation, we used the subaperture stitching DOE which is already presented in Fig. 11 to perform the imaging tests.

The imaging performance was primarily tested by introducing zero stitching error, and the ideal telescope system provides a uniform star point with a diameter of nearly 150 μm using a He-Ne laser (632.8 nm). Next, the subaperture telescope was tested by introducing stitching errors to the outermost belt (i.e., C belt in Fig. 11). To be more specific, two axial offset errors of 5 mm and 7 mm were introduced in C belt. Here, an axial stitching error of 5 mm is minor to the error tolerance (i.e., the axial offset error tolerance is 5.06 mm), and an axial stitching error of 7 mm is greater than the error tolerance. Then, the subaperture stitching diffractive telescope with a 5 mm axial stitching error presented a uniform star point like the stitching-error-free case. However, the subaperture stitching diffractive telescope with a 7 mm axial stitching error gives a distorted star point which means the imaging quality is deteriorated [31]. Apart from the star point test, we also performed the resolution bar test by using an LED with its wavelength ranging from 620 nm to 640 nm. A 75 cy/mm resolution was obtained if the telescope has no stitching error or the stitching error is smaller than the error tolerance. On the other hand, the resolution is decreased to 71 cy/mm once the stitching error is 7 mm in C belt [31]. At this moment, the star points and the resolution bar tests prove the correctness of the stitching theory in a subaperture stitching diffractive telescope.

4.4. Compound diffractive telescope

Even though the subaperture stitching DOE is feasible to provide high-resolution imaging in a diffractive telescope, a large aperture will limit a wide FOV according to Eq. (18). Therefore, inspired by the compound eye structure [100–102], compound DOEs are investigated [103–106] and the compound diffractive telescope is proposed to broad the telescope FOV [24,107]. The principle of compound optics is that an optical element can be separated into numbers of small uniform sections and each section is tilted a certain angle to the optical axis. Then, the final image is the combination of all images received by all tilted sections and the FOV is enlarged. By applying compound optics, Liu et al. designed a 50 mm diameter compound diffractive telescope [24]. They first demonstrated that the error tolerance for the eyepiece tilting within their 50 mm diameter telescope system is relative loose (i.e., ± 2°), so a reasonable eyepiece tilting is acceptable. Under this scenario, the full aperture eyepiece in this telescope was replaced by 21 small eyepieces with each eyepiece being tilted 0.2° to its adjacent piece with respect to the optical axis. In this case, the outermost piece is tilted by 2° and it still satisfies the tilting error tolerance. Therefore, the full FOV of the compound diffractive telescope could reach 4.2°. On the other hand, a same diffractive telescope without using compound eyepiece architecture only has a narrow FOV of 0.2°. In fact, the compound telescope FOV is restricted by the eyepiece tilting tolerance. After the optical design, the system was experimentally implemented. Instead of using the whole 21 eyepieces, they applied four compound eyepieces by putting two eyepieces at 0° and 0.2° to the optical axis, and the remaining two eyepieces were located at the edge of the compound optics at 1.8° and 2°. Later, by using a 632.8 nm He-Ne laser, the star points and the resolution bar images were measured at both: (i) the 0° compound eyepiece channel and (ii) the 2° compound eyepiece channel. The star point images in both channels present uniform distributions. However, the star point in the 0° channel is more homogeneous than the 2° channel because of the system astigmatism. Moreover, the resolution bar test was implemented and both channels can perform clear imaging at the 200 cy/mm spatial frequency. The resolution bar test results of both channels are given in Fig. 18 for the sake of clarity.

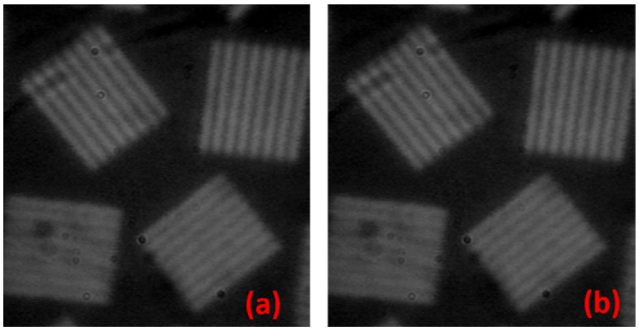

Fig. 18. The resolution bar test results of (a) 0° channel and (b) 2° channel [24].

4.5. Compact diffractive telescope

Note that most large aperture diffractive telescopes are finally investigated to be used for space mission, so they always need a large aperture and therefore lead to a practically long optical scheme. For instance, “Gen II” has a total optical track of 19 m, MOIRE prototype is 27 m long and the 300 mm diameter subaperture telescope proposed by Zhang et al. has a total length of even more than 35 m. Such long optical tracks will inevitably introduce air turbulence to the ground-based tests [108,109]. Moreover, the long telescope sketch requires an extremely precise system calibration which is costly and complicated [110,111]. Under this scenario, a compact diffractive telescope system was proposed by Zhang et al. to compact the whole system length [32]. Consequently, the air turbulence in the ground-based test can be eliminated and a better optical performance, especially an enhanced image contrast can be obtained.

The compacted diffractive telescope contains two major sections as a large diameter primary DOE and a chromatic dispersion corrector. Differ from the traditional diffractive telescope, a relay optics of positive power is inserted between the two sections to offer a strong convergence (see Section 2.2). To be more specific, Zhang et al. used aspherical mirrors as the relay optics, and they sketched a Cassegrain diffractive telescope. The telescope sketch is presented in Fig. 19 [32].

In Fig. 19, the light will first pass through the primary DOE and then it is reflected by both mirrors (i.e., the aspherical mirror and the second spherical mirror in Fig. 19) and finally entering the chromatic dispersion corrector. The second mirror is confined in the primary DOE which has a hole in its center. Here, the aspherical mirror and the second mirror demonstrate a Cassegrain scheme. Thus, these two reflections provided by the two mirrors can dramatically reduce the telescope length without introducing any chromatic aberration. Afterwards, the dispersed light is corrected by the corrector DOE and finally it is converged into the CCD by the convergence lens. Under this scenario, a compact telescope was experimentally implemented, and the diameter is designed as 300 mm with the total length as 1.276 m. Later, in order to compare the image quality of the compact telescope with a traditional diffractive telescope (i.e., telescopes without the Cassegrain system), a same 300 mm diameter diffractive telescope was also

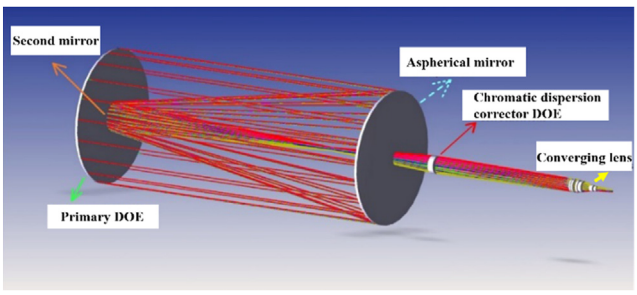

Fig. 19. System sketch of the Cassegrain compact diffractive telescope [32].

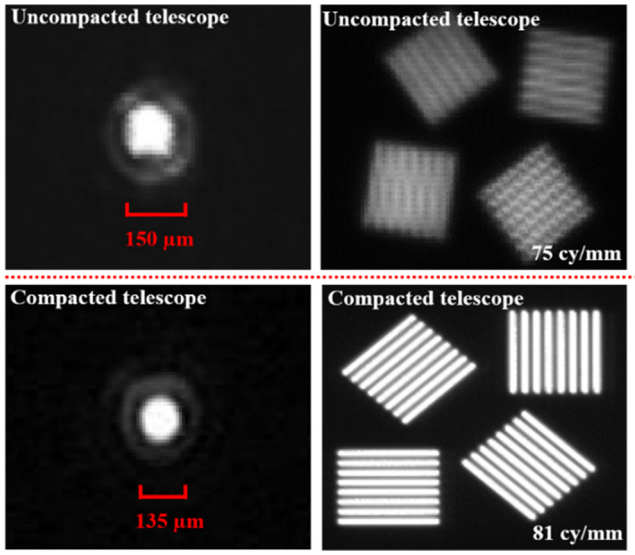

Fig. 20. Star point and resolution bar tests of the compacted Cassegrain diffractive telescope and the uncompacted diffractive telescope [32].

implemented (see Fig. 17), but the total system track at this time is longer than 35 m. We can easily deduce from the two systems that the length of the compacted telescope system is dramatically reduced. What is more, the star points and the resolution bars are tested by both the Cassegrain compacted diffractive telescope and the uncompacted telescope. The star points are obtained by using a 632. 8 nm He-Ne laser and the resolution bars are tested by implementing a LED with its wavelength ranges from 620 nm to 640 nm. From the testing results, we find that the star point image of the Cassegrain compacted diffractive telescope has a better uniformity than that of the normal telescope. Moreover, the resolution bar tests reveal that the Cassegrain telescope could provide a better visualization than the normal telescope. The results of the star point and the resolution bar test are given in Fig. 20. The star points have the diameters of ~135 μm and ~150 μm for the Cassegrain diffractive telescope and the normal diffractive telescope, respectively. Moreover, the resolution bar tests present two resolutions as 75 cy/mm and 81 cy/mm. Based on the testing results, the advantage of the compacted diffractive telescope is clearly proved. Specifically, a Cassegrain scheme based diffractive telescope not only provides a more compact architecture to eliminate the air turbulence, but also its imaging quality is enhanced compared to the normal uncompacted diffractive telescope.

At this moment, we have reviewed five different types of diffractive telescope systems in the above sections. In particular, the system parameters and the imaging ability of each diffractive telescope are presented. Hence, it is mandatory to reveal both the advantages and the shortcomings of each system, so that we can select the proper telescope system for particular applications. To do so, we compare all five abovementioned telescope systems in Table 2 and give their advantages and the shortcomings.

Table 2 presents the advantages and the shortcomings of any telescope system. By considering the characteristic of any diffractive telescope, we can select the proper system for particular application. For instance, if a space diffractive telescope is required, we should implement a photon sieve into the telescope so that we can decrease the launching weight. Moreover, subaperture stitching technique is also desired because they can guarantee a large aperture, which is crucial in astronomy imaging. Next, if a wide FOV imaging is necessary, we can always introduce compound eye structure into the telescope, and finally, we should compact the whole telescope system to ease the launching difficulty. Nowadays, such techniques have been proven feasible for ground-based tests in the laboratory, the potential application in space telescope still requires further explore.

5. Conclusion

In this paper, we thoroughly overview the techniques to implement a large aperture diffractive telescope. Preliminarily, we prove that the chromatic aberration is the most critical challenge in any diffractive telescope and therefore the Schupmann chromatic aberration correction theory is proposed to guide the telescope system design. Under this scenario, the well-known four optical elements based diffractive telescope is introduced and two system design conditions are demonstrated as Eqs. (7) and (8). To be more specific, these four elements include a large aperture primary diffractive lens, a field lens, a second DOE chromatic aberration corrector and an eyepiece. Afterwards, we also verify that by inserting a relay optical system between the primary diffractive lens and the field lens, the whole telescope sketch could be dramatically compacted without deteriorating the image quality. Once the telescope system scheme is determined, we introduce the techniques to fabricate DOEs used in diffractive telescope systems. We demonstrate that the most suitable method to obtain the DOEs is optical lithography or laser direct writing. Once the DOE fabrication technique is determined, we describe the fabrication of either Fresnel zone plates (FZP) or photon sieves on silica or membrane substrate. At last, to perform high-resolution imaging, we propose subaperture stitching to enlarge the primary DOE aperture, so that the imaging resolution could be further improved.

Once we present the design principle of a diffractive telescope and the practical methods to fabricate the DOE, we then review different types of diffractive telescopes by focusing on their particular applications. In this paper, five different kinds of diffractive telescopes are reviewed. FZP diffractive telescopes demonstrate their ability to be utilized in different wavelength ranges and this is especially favored in ultra UV imaging. Membrane diffractive telescopes and subaperture telescopes prove the potential possibility for space mission because they not only can guarantee extremely lightweight launching, but also, they can provide meter size class aperture which is crucial in astronomical

Table 2
The advantages and shortcomings of each reviewed diffractive telescope systems. Here, symbol "+" means the advantages, and symbol "–" is used to present the shortcomings.

FZP based telescope	+ We can perform achromatic imaging in different spectral ranges (i.e., UV, IR, visible light). – The telescope has a great optical length and thus the imaging quality could be deteriorated.
Photon sieve telescope	+ The system weight could be decreased by using membrane photon sieves. – The diffraction efficiency of a photon sieve is low.
Subaperture stitching telescope	+ We can obtain a large aperture primary DOE, so the imaging resolution is improved. – The subaperture stitching error will deteriorate the imaging quality.
Compound telescope	+ Large FOV imaging can be performed. – Compound eye calibration is complex.
Compact telescope	+ The system length can be compacted and thus the air fluctuation effect is avoided. – We need to introduce relay optics between the primary DOE and the corrector, so the system calibration is complicated.

observation. Finally, the concept of the compound diffractive telescope offers the feasibility to perform large FOV imaging and the compacted telescope example explicitly demonstrates a solution to overcome the inevitable air turbulence generated in the regular long optical track diffractive telescope.

In the end, we want to note that even though the existing large aperture diffractive telescopes have already proved their great abilities to perform high-resolution imaging, further investigations are still required in several aspects. For instance, the large FOV of the diffractive telescope is in fact restricted by the wide spectral bandwidth. Therefore, it is mandatory to study how to obtain large FOV imaging with a wide imaging bandwidth. Moreover, as the diffractive telescopes normally has a long optical track greater than several meters, the system calibration, especially the spatial calibration between the primary DOE and the eyepiece, must be studied. Afterwards, the high precision fabrication of the large aperture DOE, especially the pattern transformation to the flexible membrane, has to be further investigated. This is because the vast heat generated during the pattern transforming (i.e., the ion beam etching) will introduce membrane deformation and deteriorate the DOE patterns even though the membrane has a great non-zero thermal expansion coefficient. Finally, as stitching errors are inevitable during subaperture DOE stitching and it will deteriorate the imaging quality, the surface shape testing technique has to be developed to inspect the subaperture stitching quality so we can compensate the stitching error.

Declaration of Competing Interest

The authors declare that they have no known competing financial interests or personal relationships that could have appeared to influence the work reported in this paper.

Acknowledgements

This work is financially supported by Jilin Province Youth Leading Talent and Team Project (20160519021JH). Haolin Zhang would like to thank Miao Zhang for the helpful assistance during the manuscript preparation.

References

[1] K.P. Thompson, J.P. Rolland, Freeform optical surfaces: a revolution in imaging optical design, Opt. Photonics News 23 (6) (2012) 30–35.
[2] O. Cakmakci, B. Moore, H. Foroosh, J.P. Rolland, Optimal local shape description for rotationally non-symmetric optical surface design and analysis, Opt. Express 16 (3) (2008) 1583–1589.
[3] Y. Shimizu, S. Goto, J. Lee, S. Ito, W. Gao, S. Adachi, K. Omiya, H. Sato, T. Hisada, Y. Saito, H. Kubota, Fabrication of large-size SiC mirror with precision aspheric profile for artificial satellite, Prec Eng 37 (3) (2013) 640–649.
[4] Y. Zhang, J. Zhang, J. Han, X. He, W. Yao, Large-scale fabrication of lightweight Si/SiC ceramic composite optical mirror, Mater. Lett. 58 (7–8) (2004) 1204–1208.
[5] J.H. Bruning, D.R. Herriott, J.E. Gallagher, D.P. Rosenfeld, A.D. White, D.J. Brangaccio, Digital wavefront measuring interferometer for testing optical surfaces and lenses, Appl. Opt. 13 (11) (1974) 2693–2703.
[6] Z. Malacara, M. Servin, Interferogram Analysis for Optical Testing, CRC Press, 2016.
[7] C. Tian, S. Liu, Two-frame phase-shifting interferometry for testing optical surfaces, Opt. Express 24 (16) (2016) 18695–18708.
[8] J.D. Briers, Optical testing: a review and tutorial for optical engineers, Opt. Lasers Eng. 32 (2) (1999) 111–138.
[9] J.P. Gardner, J.C. Mather, M. Clampin, R. Doyon, M.A. Greenhouse, H.B. Hammel, J.B. Hutchings, P. Jakobsen, S.J. Lilly, K.S. Long, J.I. Lunine, The James Webb space telescope, Space Sci. Rev. 123 (4) (2006) 485–606.
[10] G.H. Sanders, The thirty meter telescope (tmt): An international observatory, J. Astrophys. Astron. 34 (2) (2013) 81–86.
[11] M. Johns, P. McCarthy, K. Raybould, A. Bouchez, A. Farahani, J. Filgueira, G. Jacoby, S. Shectman, M. Sheehan, Giant Magellan Telescope: overview, Proc. SPIE 8444 (2012) 84441H.
[12] C. Baffes, T. Mast, J. Nelson, E. Ponslet, V. Stephens, L. Stepp, E.C. Williams, Primary mirror segmentation studies for the Thirty Meter Telescope, Proc. SPIE 7018 (2008) 70180S.
[13] G. Olczak, D.J. Fischer, M. Connelly, Wells C. James, Webb Space Telescope primary mirror integration: testing the multiwavelength interferometer on the test bed telescope, Proc. SPIE 8146 (2011) 814608.
[14] R.A. Hyde, Eyeglass. 1.Very large aperture diffractive telescopes, Appl. Opt. 38 (19) (1999) 4198–4212.
[15] G. Andersen, O. Asmolova, T. Dickinson, FalconSAT-7: a membrane space telescope, Proc. SPIE 9085 (2014) 908504.
[16] R.A. Hyde, S.N. Dixit, A.H. Weisberg, M.C. Rushford, Eyeglass: a very large aperture diffractive space telescope, Proc. SPIE 4849 (2002) 28–40.
[17] E. Hinglais, A space Fresnel imager concept assessment study led by CNES for astrophysical applications, Exp. Astron. 30 (2–3) (2011) 85.
[18] D.A. Buralli, G.M. Morris, Design of two-and three-element diffractive Keplerian telescopes, Appl. Opt. 31 (1) (1992) 38–43.
[19] L. Schupmann, Die medial-fernrohre: eine neue konstruktion für grosse astronomische instrumente, BG Teubner (1899).
[20] L. Koechlin, J.P. Rivet, P. Deba, T. Raksasataya, T. Gharsa, R. Gili, Generation 2 testbed of Fresnel imager: first results on the sky, Exp. Astron. 30 (2–3) (2011) 165–182.
[21] L. Koechlin, J.P. Rivet, P. Deba, D. Serre, T. Raksasataya, R. Gili, J. David, First high dynamic range and high resolution images of the sky obtained with a diffractive Fresnel array telescope, Exp. Astron. 33 (1) (2012) 129–140.
[22] L. Koechlin, M. Yadallee, T. Raksasataya, A. Berdeu, New progress on the Fresnel imager for UV space astronomy, Astrophys. Space Sci. 354 (1) (2014) 147–153.
[23] R. Wilhem, K. Laurent, Improvements on Fresnel arrays for high contrast imaging, Exp. Astron. 45 (1) (2018) 21–40.
[24] H. Liu, Z. Lu, J. Yue, H. Zhang, The characteristics of compound diffractive telescope, Opt. Express 16 (20) (2008) 16195–16201.
[25] G. Andersen, D. Tullson, Broadband antihole photon sieve telescope, Appl. Opt. 46 (18) (2007) 3706–12708.
[26] G. Andersen, Membrane photon sieve telescopes, Appl. Opt. 49 (33) (2010) 6391–6394.
[27] P.D. Atcheson, C. Stewart, J. Domber, K. Whiteaker, J. Cole, P. Spuhler, A. Seltzer, J.A. Britten, S.N. Dixit, B. Farmer, L. Smith, MOIRE: initial demonstration of a transmissive diffractive membrane optic for large lightweight optical telescopes, Proc. SPIE, 8442 2012, p. 84422.
[28] P. Atcheson, J. Domber, K. Whiteaker, J.A. Britten, S.N. Dixit, B. Farmer, MOIRE: ground demonstration of a large aperture diffractive transmissive telescope, Proc. SPIE, 9143 2014, p. 91431W.
[29] J.L. Domber, P.D. Atcheson, J. Kommers, MOIRE: ground test bed results for a large membrane telescope, Spacecraft Structures Conference 1510 (2014).
[30] J.M. Irvine, National imagery interpretability rating scales (NIIRS): overview and methodology, Proc. SPIE, 3128 1997, pp. 93–103.
[31] H. Zhang, H. Liu, W. Xu, A. Lizana, X. Wang, Z. Lu, Error analysis of large-diameter subaperture stitching Fresnel diffractive elements, Appl. Opt. 56 (27) (2017) 7672–7678.
[32] H. Zhang, H. Liu, A. Lizana, W. Xu, J. Caompos, Z. Lu, Methods for the performance enhancement and the error characterization of large diameter ground-based diffractive telescopes, Opt. Express 25 (22) (2017) 26662–26677.
[33] R. Barakat, Rayleigh wavefront criterion, JOSA 55 (5) (1965) 572–573.
[34] R.H. Katyl, Compensating optical systems. Part1: broadband holographic reconstruction, Appl. Opt. 11 (5) (1972) 1241–1247.
[35] J.N. Latta, Analysis of multiple hologram optical elements with low dispersion and low aberrations, Appl. Opt. 11 (8) (1972) 1686–1696.
[36] S.J. Bennett, Achromatic combinations of hologram optical elements, Appl. Opt. 15 (2) (1976) 542–545.
[37] T. Stone, N. George, Hybrid diffractive-refractive lenses and achromats, Appl. Opt. 27 (14) (1988) 2960–2971.
[38] C.G. Blough, M. Rossi, S.K. Mack, R.L. Michaels, Single-point diamond turning and replication of visible and near-infrared diffractive optical elements, Appl. Opt. 36 (20) (1997) 4648–4654.
[39] C.J. Li, Y. Li, X. Gao, C.V. Duong, Ultra-precision machining of Fresnel lens mould by single-point diamond turning based on axis B rotation, Int. J. Adv. Manuf. Technol. 77 (5–8) (2015) 907–913.
[40] X. Zhang, K. Liu, X. Shan, Y. Liu, Roll-to-roll embossing of optical linear Fresnel lens polymer film for solar concentration, Opt. Express 22 (107) (2014) A1835–A1842.
[41] W. Chao, J. Kim, S. Rekawa, P. Fischer, E.H. Anderson, Demonstration of 12 nm resolution Fresnel zone plate lens based soft X-ray microscopy, Opt. Express 17 (20) (2009) 17669–17677.
[42] K. Keskinbora, C. Grévent, M. Bechtel, M. Weigand, E. Goering, A. Nadzeyka, L. Peto, S. Rehbein, G. Schneider, R. Follath, J. Vila-Comamala, Ion beam lithography for Fresnel zone plates in X-ray microscopy, Opt. Express 21 (10) (2013) 11747–11756.
[43] Y. Li, N. Zheng, H. Li, J. Hou, X. Lei, X. Chen, Z. Yuan, Z. Guo, J. Wang, Y. Guo, Q. Xu, Morphology and distribution of subsurface damage in optical fused silica parts: Bound-abrasive grinding, Appl. Surf. Sci. 257 (6) (2011) 2066–2073.
[44] Z. Zhang, C. Guo, R. Wang, H. Hu, X. Zhou, T. Liu, D. Xue, X. Zhang, F. Zhang, X. Zhang, Hybrid-level Fresnel zone plate for diffraction efficiency enhancement, Opt. Express 25 (26) (2017) 33676–122687.
[45] L.F. Thompson, C.G. Willson, M.J. Bowden, Introduction to microlithography, 1983.
[46] E. Bricchi, J.D. Mills, P.G. Kazansky, B.G. Klappauf, J.J. Baumberg, Birefringent Fresnel zone plates in silica fabricated by femtosecond laser machining, Opt. Lett. 27 (24) (2002) 2200–2202.
[47] P. Srisungsitthisunti, O.K. Ersoy, X. Xu, Volume Fresnel zone plates fabricated by femtosecond laser direct writing, Appl. Phys. Lett. 90 (1) (2007) 011104.
[48] P. Srisungsitthisunti, O.K. Ersoy, X. Xu, Laser direct writing of volume modified Fresnel zone plates, JOSA B 24 (9) (2007) 2090–2096.

[49] K. Kodate, H. Takenaka, T. Kamiya, Fabrication of high numerical aperture zone plates using deep ultraviolet lithography, Appl. Opt. 23 (3) (1984) 504–507.
[50] K. Kodate, T. Kamiya, Y. Okada, H. Takenaka, Focusing characteristics of high-efficiency Fresnel zone plate fabricated by deep ultraviolet lithography, Jpn. J. Appl. Phys. 25 (2R) (1986) 223.
[51] I.J. Djomehri, T.A. Savas, H.I. Smith, Zone-plate-array lithography in the deep ultraviolet, J Vac Sci Techn B Microelectron Nanometer Struct Process Meas Phenom 16 (6) (1998) 3426–3429.
[52] T. Fujita, H. Nishihara, J. Koyama, Fabrication of micro lenses using electron-beam lithography, Opt. Lett. 6 (12) (1981) 613–615.
[53] S. Gorelick, J. Vila-Comamala, V.A. Guzenko, R. Barrett, M. Salomé, C. David, High-efficiency Fresnel zone plates for hard X-rays by 100 keV e-beam lithography and electroplating, J. Synchrotron Radiat. 18 (3) (2011) 442–446.
[54] A. Nadzeyka, L. Peto, S. Bauerdick, M. Mayer, K. Keskinbora, C. Grévent, M. Weigand, M. Hirscher, G. Schütz, Ion beam lithography for direct patterning of high accuracy large area X-ray elements in gold on membranes, Microelectron. Eng. 98 (2012) 198–201.
[55] J. Overbuschmann, J. Hengster, S. Irsen, T. Wilhein, Fabrication of Fresnel zone plates by ion-beam lithography and application as objective lenses in extreme ultraviolet microscopy at 13 nm wavelength, Opt. Lett. 37 (24) (2012) 5100–5102.
[56] K. Keskinbora, U.T. Sanli, M. Baluktsian, C. Grévent, M. Weigand, G. Schütz, High-throughput synthesis of modified Fresnel zone plate arrays via ion beam lithography, Beilstein J. Nanotechnol. 9 (2018) 2049.
[57] J.A. Britten, S.N. Dixit, M. DeBruyckere, D. Steadfast, J. Hackett, B. Farmer, G. Poe, B. Patrick, P.D. Atcheson, J.L. Domber, A. Seltzer, Large-aperture fast multilevel Fresnel zone lenses in glass and ultrathin polymer films for visible and near-infrared imaging applications, Appl. Opt. 53 (11) (2014) 2312–2316.
[58] M.T. Gale, Direct Writing of Continuous-relief Micro-optics, Taylor & Francis, London, 1997, pp. 87–126.
[59] C. Pruss, S. Reichelt, H.J. Tiziani, V.P. Korolkov, Metrological features of diffractive high-efficiency objectives for laser interferometry, in: Proc. SPIE, nternational Society for Optics and Photonics, vol. 4900, 2002, pp. 8442–84422.
[60] J.H. Burge, Applications of computer-generated holograms for interferometric measurement of large aspheric optics, Proc. SPIE, 2576 1995, pp. 258–269.
[61] J.P. Bowen, R.L. Michaels, C.G. Blough, Generation of large-diameter diffractive elements with laser pattern generation, Appl. Opt. 36 (34) (1997) 8970–8975.
[62] L. Kipp, M. Skibowski, R.L. Johnson, R. Berndt, R. Adelung, S. Harm, R. Seemann, Sharper images by focusing soft X-rays with photon sieves, Nature 414 (6860) (2001) 184.
[63] G. Andersen, Large optical photon sieve, Opt. Lett. 30 (22) (2005) 2976–2978.
[64] X. Zhao, F. Xu, J. Hu, C. Wang, Broadband photon sieves imaging with wavefront coding, Opt. Express 23 (13) (2015) 16812–16822.
[65] X. Zhao, J. Hu, Y. Lin, F. Xu, X. Zhu, D. Pu, L. Chen, C. Wang, Ultra-broadband achromatic imaging with diffractive photon sieves, Sci. Rep. 6 (2016) 28319.
[66] Y. Li, C. Wang, X. Zhao, F. Xu, C. Wang, Multispectral and large bandwidth achromatic imaging with a single diffractive photon sieve, Opt. Express 26 (16) (2018) 21141–21152.
[67] M.N. Julian, D.G. MacDonnell, M.C. Gupta, Fabrication of photon sieves by laser ablation and optical properties, Opt. Express 25 (25) (2017) 31528–31538.
[68] M.N. Julian, D.G. MacDonnell, M.C. Gupta, Flexible binary phase photon sieves on polyimide substrates by laser ablation, Opt. Lett. 43 (10) (2018) 2368–2371.
[69] I.M. Barton, J.A. Britten, S.N. Dixit, L.J. Summers, I.M. Thomas, M.C. Rushford, K. Lu, R.A. Hyde, M.D. Perry, Fabrication of large-aperture lightweight diffractive lenses for use in space, Appl. Opt. 40 (4) (2001) 447–451.
[70] J.T. Early, R. Hyde, R.L. Baron, Twenty-meter space telescope based on diffractive Fresnel lens, Proc. SPIE 5166 (2004) 148–157.
[71] O. Asmolova, G. Andersen, M.E. Dearborn, M.G. McHarg, T. Quiller, T. Murphey, Optical analysis of a membrane photon sieve space telescope, Proc. SPIE, 8739 2013, p. 87390C.
[72] J. Jiao, B. Wang, C. Wang, Y. Zhang, J. Jin, Z. Liu, Y. Su, N. Ruan, Study on high resolution membrane-based diffractive optical imaging on geostationary orbit, Int. Arch. Photogramm. Remote Sens. Spat. Inf. Sci. 42 (2017) 371.
[73] W. Tandy, P. Atcheson, J. Domber, A. Seltzer, MOIRE gossamer space telescope-structural challenges and solutions, in: 53rd AIAA/ASME/ASCE/AHS/ASC Structures, Structural Dynamics and Materials Conference 20th AIAA/ASME/AHS Adaptive Structures Conference 14th AIAA 2012; 1670.
[74] G. Jin, J. Yan, H. Liu, X. Zhong, Y. Yan, Flat-stitching error analysis of large-aperture photon sieves, Appl. Opt. 53 (1) (2014) 90–95.
[75] T.J. Cornwell, A novel principle for optimization of the instantaneous Fourier plane coverage of correction arrays, IEEE Trans. Antennas Propag. 36 (8) (1988) 1165–1167.
[76] M.J. Golay, Point arrays having compact, nonredundant autocorrelations, JOSA 61 (2) (1971) 272–273.
[77] L. Koechlin, P. Deba, T. Raksasataya, Astrophysical targets of the Fresnel diffractive imager, Proc. SPIE, 10566 2017, p. 1056602.
[78] D. Serre, P. Deba, L. Koechlin, Fresnel interferometric imager: ground-based prototype, Appl. Opt. 48 (15) (2009) 2811–2820.
[79] L. Koechlin, D. Serre, P. Deba, R. Pelló, C. Peillon, P. Duchon, A.I. de Castro, M. Karovska, J.M. Désert, D. Ehrenreich, G. Hebrard, The Fresnel interferometric imager, Exp. Astron. 23 (1) (2009) 379–402.
[80] T. Raksasataya, P. Deba, J.P. Rivet, R. Gili, D. Serre, Koechlin L. Fresnel diffractive imager: instrument for space mission in the visible and uv, Proc. SPIE, 7732 2010, p. 77322D.
[81] T. Raksasataya, A.I. de Castro, L. Koechlin, J.P. Rivet, A space Fresnel Imager for ultra-violet astrophysics: example on accretion disks, Exp. Astron. 30 (2–3) (2011) 183.
[82] D. Serre, L. Koechlin, P. Deba, The Fresnel Imager: learning from ground-based generation I prototype, Exp. Astron. 30 (2–3) (2011) 137–147.
[83] J.P. Rivet, L. Koechlin, T. Raksasataya, P. Deba, R. Gili, Fresnel imager testbeds: setting up, evolution, and first images, Exp. Astron. 30 (2–3) (2011) 149.
[84] W. Roux, L. Koechlin, Diffractive telescope for protoplanetary disks study in UV. in SF2A- 2015, Proceedings of the Annual meeting of the French Society of Astronomy and Astrophysics, 2015, pp. 289–292.
[85] S. Roose, Y. Stockman, D. Derauw, L. Datashvlli, H. Baier, The challenges for large light-weight diffractive lenses for space telescopes, Proc. SPIE, 10563 2017, p. 105635Y.
[86] B. Qi, L. Wang, Z. Cui, J. Bian, S. Xiang, H. Ma, B. Fan, Opto-mechanical design and development of a 460mm diffractive transmissive telescope, Proc. SPIE, 10456 2018, p. 104565I.
[87] D. Liu, L. Wang, W. Yang, S. Wu, B. Fan, F. Wu, Stray light characteristics of the diffractive telescope system, Opt. Eng. 57 (2) (2018) 025105.
[88] Q. Kong, S. Wang, P. Yang, G. Tang, W. Yang, X. Yu, B. Pang, K. Yang, Y. Liu, B. Xu, Aberration correction of Fresnel zone lenses telescope based on adaptive optics system, Opt. Eng. 57 (6) (2018) 063107.
[89] G. Andersen, O. Asmolov, M.E. Dearborn, M.G. McHarg, FalconSAT- 7: a membrane photon sieve CubeSat solar telescope, Proc. SPIE, 8442 2012, p. 84421C.
[90] G. Andersen, O. Asmolova, G. McHarg, M. Dearborn, T. Quiller, FalconSAT- 7: Towards Rapidly Deployable Space-based Surveillance, Air Force Academy Colorado Springs Co Dept of Physics, 2013.
[91] G. Andersen, M. Dearborn, G. McHarg, FalconSAT- 7: A Photon Sieve SOLAR Telescope, Air Force Academy Colorado Springs Co, 2011.
[92] W.A. Kleinhans, Aberrations of curved zone plates and Fresnel lenses, Appl. Opt. 16 (6) (1977) 1701–1704.
[93] J.T. Rantala, P. Äyräs, R. Levy, S. Honkanen, M.R. Descour, N. Peyghambarian, Binary-phase zone-plate arrays based on hybrid solgel glass, Opt. Lett. 23 (24) (1998) 1939–1941.
[94] S. Karimkashi, A.A. Kishk, Focusing properties of Fresnel zone plate lens antennas in the near-field region, IEEE Trans. Antennas Propag. 59 (5) (2011) 1481–1487.
[95] Z. Xiong, H. Liu, R. Chen, J. Xu, Q. Li, J. Li, W. Zhang, Illumination uniformity improvement in digital micromirror device based scanning photolithography system, Opt. Express 26 (14) (2018) 18597–18607.
[96] A. Waldbaur, B. Waterkotte, K. Schmitz, B.E. Rapp, Maskless projection lithography for the fast and flexible generation of grayscale protein patterns, Small 8 (10) (2012) 1570–1578.
[97] Q.K. Li, Y. Xiao, H. Liu, H.L. Zhang, J. Xu, J.H. Li, Analysis and correction of the distortion error in a DMD based scanning lithography system, Opt. Commun. 434 (2019) 1–6.
[98] F. Watt, A.A. Bettiol, J.A. Van Kan, E.J. Teo, M.B. Breese, Ion beam lithography and nanofabrication: a review, Int. J. Nanosci. 4 (03) (2005) 269–286.
[99] D. Waller, L. Campbell, J.L. Domber, D. Putnam, R.T. Thompson, MOIRE primary diffractive optical element structure deployment testing, in: 2nd AIAA Spacecraft Structures Conference, vol. 1836, 2015.
[100] J. Duparré, P. Schreiber, A. Matthes, E. Pshenay-Severin, A. Bräuer, A. Tünnermann, R. Völkel, M. Eisner, T. Scharf, Microoptical telescope compound eye, Opt. Express 13 (3) (2005) 889–903.
[101] H. Zhang, L. Li, D.L. McCray, S. Scheiding, N.J. Naples, A. Gebhardt, S. Risse, R. Eberhardt, A. Tünnermann, Y.Y. Allen, Development of a low cost high precision three-layer 3D artificial compound eye, Opt. Express 21 (19) (2013) 22232–22245.
[102] W.B. Lee, H. Jang, S. Park, Y.M. Song, H.N. Lee, COMPU-EYE: a high resolution computational compound eye, Opt. Express 24 (3) (2016) 2013–2026.
[103] A. Kuyumchyan, A.A. Isoyan, E.V. Shulakov, V.V. Aristov, M. Kondratenkov, A.A. Snigirev, I. Snigireva, A. Souvorov, K. Tamasaku, M. Yabashi, T. Ishikawa, High-efficiency and low-absorption Fresnel compound zone plates for hard X-ray focusing, Proc. SPIE, 4783 2002, pp. 92–97.
[104] O. Von Hofsten, M. Bertilson, J. Reinspach, A. Holmberg, H.M. Hertz, U. Vogt, Sub-25-nm laboratory x-ray microscopy using a compound Fresnel zone plate, Opt. Lett. 34 (17) (2009) 2631–2633.
[105] S. Zhang, L. Zhou, C. Xue, L. Wang, Design and simulation of a superposition compound eye system based on hybrid diffractive-refractive lenses, Appl. Opt. 56 (26) (2017) 7442–7449.
[106] Y. Cheng, J. Cao, Q. Hao, F. Zhang, S. Wang, W. Xia, L. Meng, Y. Zhang, H. Yu, Compound eye and retina-like combination sensor with a large field of view based on a space-variant curved micro lens array, Appl. Opt. 56 (12) (2017) 3502–12509.
[107] Z. Lu, N. Zhang, H. Liu, F. Li, Q. Sun, Compound telescope, Proc. SPIE, 6289 2006, p. 628910.
[108] F. Roddier, V The effects of atmospheric turbulence in optical astronomy, Progress in Optics 19 (1981) 281–376.
[109] Z. Cao, Q. Mu, L. Hu, D. Li, Z. Peng, Y. Liu, L. Xuan, Preliminary use of nematic liquid crystal adaptive optics with a 2.16-meter reflecting telescope, Opt. Express 17 (4) (2009) 2530–2537.
[110] P.A. Lightsey, James Webb Space Telescope: a large deployable cryogenic telescope in space, Proc. SPIE, 6720 2007, p. 67200E.
[111] P.A. Lightsey, C.B. Atkinson, M.C. Clampin, L.D. Feinberg, James Webb Space Telescope: large deployable cryogenic telescope in space, Opt. Eng. 51 (1) (2012) 011003.